RSC Applied Polymers

GOLD OPEN ACCESS

ROYAL SOCIETY OF CHEMISTRY

ROYAL SOCIETY OF CHEMISTRY

rsc.li/RSCApplPolym

ARTICLE

Flexible PVDF/ZnFe₂O₄ nanofibers-based Magneto-Mechano-Electrical Generator for Energy Harvesting and Sensing Applications

Durga Prasad Pabba[a][†], Nayak Ram[b], J. Kaarthik[c], Vijayabhaskara Rao Bhaviripudi[d], Sandeep Kumar Yadav[e], M. Satthiyaraju[f], R.V. Mangalaraja[g,h], Radhamanohar Aepuru[i][†], Annapureddy Venkateswarlu[b][†]

The increasing demand for reliable energy sources to power electronic devices in remote and non-contact environments has driven advancements in energy harvesting technologies. Among these, magneto-mechano-electric (MME) harvesters stand out for their ability to generate energy through non-contact magnetic interactions. In this study, we developed self-biasing, multi-mode flexible MME generators based on PVDF/ZnFe2O4 fibers composites for efficient energy harvesting and sensing applications. The ZnFe₂O₄ magnetic nanofiber fillers have been synthesized and optimized using an electrospinning technique followed by heat treatment. Flexible PVDF/ZnFe₂O₄ fiber composites have been fabricated using the electrospinning process. X-ray diffraction (XRD) and Fourier-transform infrared (FTIR) spectroscopy demonstrated an improved ferroelectric β-phase in PVDF, attributed to the integration of ZnFe₂O₄ nanofibers. The resulting PVDF/ZnFe₂O₄ composite exhibited multiferroic magnetoelectric (ME) properties, as demonstrated by its ferroelectric and magnetic behavior. The composite was used to fabricate versatile MME generators, which achieved an impressive output voltage of 7.8 V and a power density of 106 μW/m² under a low alternating current (AC) magnetic field of 6 Oe, about four times higher than a neat PVDF-based MME generator. Furthermore, the device achieved a high magnetoelectric voltage coefficient (α_{MME}) of 130 V cm⁻¹ Oe⁻¹ without a magnetic bias direct current (DC) field. The developed MME generator effectively harvested weak parasitic magnetic noise from various electrical appliances and successfully charged multiple capacitors. Beyond energy harvesting, the device functioned as a magnetic and stress sensor, demonstrating significant potential for applications in wireless sensor networks and remote powering solutions.

1. Introduction

Exploring innovative materials and methods for harvesting energy from environmental waste sources, such as mechanical vibrations and stray magnetic fields, is fundamental to advancing sustainable technologies [1,2]. Magneto-Mechano-Electric (MME)

[a]Departamento de Electricidad, Facultad de Ingeniería, Universidad Tecnológica Metropolitana, Santiago, 7800002, Chile.
[b]Flexible and Multifunctional Materials Device Lab, Department of Physics, National Institute of Technology, Tiruchirappalli, 620015, India.
[c]Department of Physics, SRM University – AP, Amaravati 522 502, Andhra Pradesh, India
[d]Departamento de física, Universidad Tecnológica Metropolitana, Santiago, 7800002, Chile.
[e]Department of Physics, National Institute of Technology, Tiruchirappalli, Tamil Nadu, 620015, India.
[f]Department of Mechanical Engineering, SRM Institute of Science and Technology, Vadapalani campus, Vadapalani, Chennai -600026.
[g]Faculty of Engineering and Sciences, Universidad Adolfo Ibáñez, Diagonal las Torres 2640, Peñalolén 7941169, Santiago, Chile.
[h]Vicerrectoría de Investigación e Innovación, Universidad Arturo Prat, Avenida Arturo Prat 2120, Iquique 1110939, Chile.
[i]Departamento de Ingeniería Mecánica, Facultad de Ciencias Físicas y Matemáticas, Universidad de Chile, Santiago, Chile.
†Corresponding authors, E-mail: dpabba@utem.cl, venkata.aepuru@uchile.cl, annp@nitt.edu
Supplementary Information available: [details of any supplementary information available should be included here]. See DOI: 10.1039/x0xx00000x

devices are a recent addition to the array of energy harvesting technologies complementing piezoelectric nanogenerators (PENGs) and triboelectric nanogenerators (TENGs) [3,4]. The ability to harness abundant low-frequency stray magnetic energy, especially at frequencies around 50/60 Hz, offers a promising opportunity for efficiently converting magnetic energy into electrical power. This approach allows electrical energy generation without requiring an external force, instead utilizing a stray magnetic field produced by common electrical appliances [5]. As a result, MME devices have emerged as a focal point for their promising applications in energy harvesting. However, research on MME-based energy harvesters remains limited compared to PENGs and TENGs, mainly due to their lower output and the scarcity of suitable environmental magnetic sources[6].

Previous studies have primarily focused on ceramic or lead-based MME devices known for their brittleness and toxic properties[7,8]. Therefore, it is essential to investigate flexible polymer-based MME devices for energy harvesting. Recently, several studies have explored flexible polymer-based MME generators. For example, Song et al. [7] developed a cellulose P(VDF-TrFE)-nanocrystal (CNC)@CoFe₂O₄ nanohybrid composite generator that achieved an output voltage of 218 mV. Another study introduced a flexible poly(vinylidene fluoride) (PVDF)-CoFe₂O₄ (CFO)@BaTiO₃ MME generator, which generated 4.7 V at 5 kOe and was designed for magnetic sensor applications. A PVDF/barium calcium zirconium titanate (BCZT) composite films-based MME generator produced an

output voltage of 3.3 V [9]. Our research group designed and optimized flexible magnetoelectric (ME) generators using lead-free piezoelectric microfibers, specifically PVDF-AlN and PVDF-BCZT, integrated onto magnetostrictive Metglas layers in cantilever structures. This approach significantly enhanced the output performance, with the harvested voltage ranging from a few millivolts (mV) to several tens of volts, corresponding to power densities from nanowatts (nW) to microwatts (μW) [10,11].

PVDF, a semi-crystalline polymer, is highly regarded as an exceptional piezoelectric material, celebrated for its flexibility, straightforward processing, and environmentally friendly, non-toxic properties. PVDF exhibits five distinct crystalline phases: α, β, γ, δ, and ε. The β-phase is particularly noteworthy for its strong piezoelectric properties, which arise from its substantial dipole moment per unit cell. This phase induces spontaneous polarization under an electric field when the material undergoes structural deformation [12,13]. The polarization primarily results from the alignment of C-F dipoles in an all-trans (TTTT) configuration, oriented perpendicular to the C-C chain axis.

Achieving the β-phase is critical for producing PENGs and can be accomplished through various processing techniques such as spin-coating, drawing, poling, annealing, and electrospinning [14,15]. Additionally, the β-phase can be induced by incorporating nanofillers into PVDF, including ceramic materials, metal nanoparticles, magnetic materials, and biomaterials. Zinc ferrite ($ZnFe_2O_4$) has emerged as a promising nanofiller for inducing the β-phase in PVDF while also facilitating potential magnetoelectric (ME) coupling [16]. This is due to its unique properties, including high electrical conductivity, magnetic behavior, and straightforward synthesis routes.

This study presents a novel composite MME generator made from $PVDF/ZnFe_2O_4$ nanofibers, characterized by high flexibility, non-toxicity, and durability. Beyond energy harvesting, the composite MME generator also functions as a magnetic field sensor, even at low alternating current (AC) field strengths. Additionally, it is suitable for hybrid multi-mode energy harvesting. This multifunctionality highlights the versatility and potential applications of the developed composite MME generator, signaling promising advancements in both energy harvesting and sensing technologies. This study aims to provide an in-depth exploration of the fabrication, characterization, and potential applications of the composite MME device generator in detail, emphasizing its significance in sustainable energy technologies and sensor applications.

2. Experimental

2.1 Materials

Polyvinylidene fluoride (PVDF) with a molecular weight of 534,000 was procured from Sigma Aldrich. The starting materials, including N, N-Dimethylformamide (DMF, 99.8% purity), acetone, zinc nitrate hexahydrate ($Zn(NO_3)_2 \cdot 6H_2O$, 98.95% purity), iron nitrate nonahydrate ($Fe(NO_3)_3 \cdot 9H_2O$, 99.99% purity), and ethanol, were sourced from Merck, India, and utilized without any additional purification.

2.2 Synthesis of magnetic $ZnFe_2O_4$ nanofibers

To synthesize $ZnFe_2O_4$ nanofibers, a metal nitrate solution was prepared by dissolving zinc nitrate hexahydrate and iron nitrate nonahydrate in 1 mL of DMF at a molar ratio of 1:2. Separately, a 12 wt% polyvinylpyrrolidone (PVP) solution was also prepared by dissolving PVP in ethanol. Both solutions were stirred independently

for 2 h. Subsequently, the metal nitrate/DMF solution was gradually added to the PVP/ethanol solution, and the resulting mixture was stirred for an additional 3 h to ensure homogeneity. The precursor solution was loaded into a 10 mL Hamilton plastic syringe fitted with a 0.34 mm metal needle connected to a high-voltage power supply. Electrospinning was conducted at room temperature (RT) with a flow rate of 0.6 mL/h and an applied voltage of 20 kV. The as-spun nanofibers were collected on aluminum (Al) foil attached to a collector 15 cm below the syringe needle tip. Finally, the collected nanofibers were calcined at 700°C and 800°C for 2 h with a heating rate of 2 °C/min. to obtain highly crystalline $ZnFe_2O_4$ nanofibers, designated as ZF7 nanofibers and ZF8 nanofibers, respectively. The synthesis temperatures of 700°C and 800°C for $ZnFe_2O_4$ nanofibers were chosen based on previous studies that suggest these temperatures facilitate the formation of phase-pure $ZnFe_2O_4$ with optimal crystallinity and morphology for enhancing the electrostatic and piezoelectric properties [17,18]. At 700°C, the material is expected to undergo a partial phase transition, while at 800°C, better crystallization and larger grain sizes are achieved, improving the electrostatic interactions when combined with PVDF. While a parametric study was not explicitly conducted in this work, the selected temperatures are consistent with literature reports on the synthesis of $ZnFe_2O_4$ nanofibers and their use in composite systems. Future work could explore a detailed parametric study to optimize these conditions further.

2.3 Synthesis of piezoelectric PVDF fiber mat

An 18 wt.% PVDF solution was prepared by dissolving the polymer in a 1:1 blend of DMF and acetone to fabricate the PVDF fiber mat. The mixture was heated to 50 °C and stirred for 5 hours to ensure thorough dissolution. Subsequently, the solution underwent sonication for 1 hour and was loaded into a plastic syringe. Electrospinning was performed at a flow rate of 0.70 mL/h under an applied voltage of 20 kV. Fibers were collected on an aluminum foil substrate grounded and positioned 15 cm away from the needle tip. After 8 hours of spinning, the fiber mat was vacuum-dried at room temperature for 24 hours to eliminate residual solvents. The resulting sample was designated as PVDF FM.

2.4 Fabrication of flexible magnetoelectric (ME) fiber mats

To prepare a flexible ME composite with piezoelectric PVDF and magnetic $ZnFe_2O_4$ fibers, a solution of 18 wt.% PVDF in a 1:1 mixture of DMF and acetone was prepared by stirring at 50 °C for 5 h. Then, 15 wt.% ZF8 nanofibers were added and mixed for 30 minutes, followed by sonication for 10 minutes to ensure uniform dispersion. The final solution was electrospun under the same conditions as PVDF FM to produce the flexible ME composite fiber mat labeled PZ15.

2.5 Characterization techniques

X-ray Diffraction (XRD): The crystal structure of the samples was examined using a *Bruker D8 Advance X-ray diffractometer* (USA) with Cu K$_{\alpha1}$ radiation (λ = 1.54056 Å). Scanning Electron Microscopy (SEM): The sample morphology was characterized using a Zeiss *GeminiSEM 360* equipped with NanoVP technology. Energy Dispersive X-ray Spectrometry (EDS): The elemental composition was analyzed using an *Aztec system from Oxford Instruments* integrated with the SEM setup. Fourier-Transform Infrared Spectroscopy (FTIR):

Journal Name

ARTICLE

Functional groups in the samples were identified using a *PerkinElmer Frontier FT-IR/FIR spectrometer*. Vibrating Sample Magnetometer (VSM): Magnetic properties were evaluated using a Lakeshore 7400-S series vibrating sample magnetometer. Electrical Measurements: The output voltage and current were monitored with a *Tektronix DPO2024B oscilloscope* and a *GW Instek GDM-9061 digital multimeter*, respectively. Output power was determined by measuring the voltage and current across different load resistances.
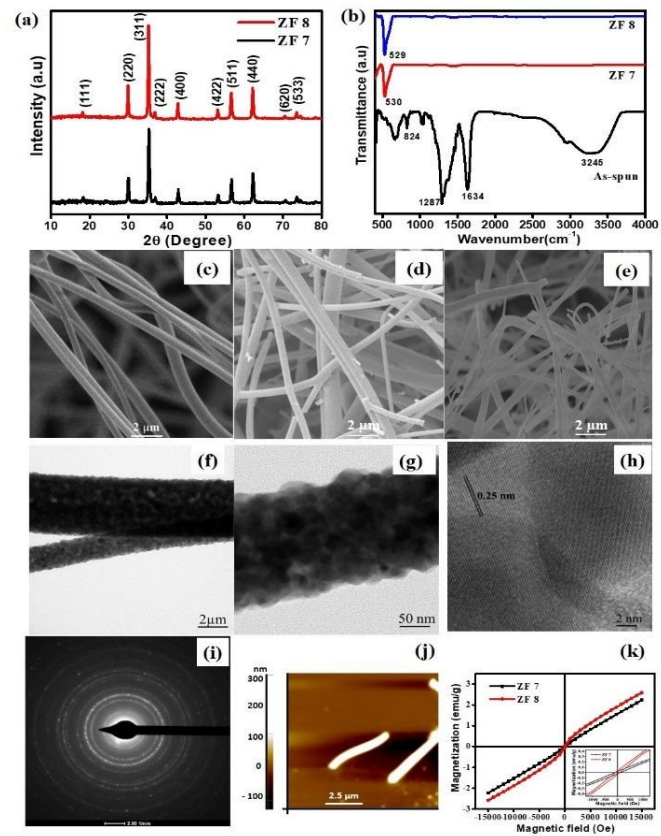
3. Results and Discussion

3.1 Characterization of ZnFe$_2$O$_4$ Nanofibers

The XRD patterns of the NF7 and NF8 nanofibers, depicted in **Fig. 1(a),** exhibit characteristic reflections corresponding to the (111), (220), (311), (222), (400), (422), (511), (440), (620), and (533) planes, verifying the cubic spinel structure of zinc ferrite. The presence of strong and sharp peaks highlights the high crystallinity of the samples, with reflections indexed according to JCPDS card no. 22-1012 [19]. The absence of any secondary or impurity peaks confirms the phase purity of the nanofibers. The estimated crystallite sizes (D) for NF7 and NF8 are 26 nm and 28 nm, respectively, while their lattice constants (a) measure 0.840 nm and 0.839 nm, closely matching the reported value of 0.844 nm [12]. The impact of calcination temperature on crystallinity is apparent from the diffraction peaks, which grow more intense, sharper, and narrower, indicating enhanced crystallinity with higher calcination temperatures.

Fig. 1: (a) XRD patterns and (b) FTIR spectra of the samples. SEM micrographs of ZnFe$_2$O$_4$ fibers: (c) as-spun, (d) ZF7, and (e) ZF8. (f-h) TEM micrographs and (i) SEAD pattern of the ZF8 sample. (j) AFM topography of ZF8 sample. (k) M-H loops of ZF7 and ZF8 samples.

Figure 1(b) presents the FTIR spectra of as-spun precursor fibers alongside ZF7 and ZF8 nanofibers, recorded across the 400–4000 cm^{-1} range. The as-spun precursor fibers display distinct peaks associated with PVP, including a characteristic absorption band at 1634 cm^{-1} corresponding to C=O stretching vibrations, phenolic-OH groups at 1287 and 3245 cm^{-1}, and an aromatic C–H group at 824 cm^{-1} [20,21]. After calcination, the decomposition of PVP results in the exclusive presence of ZnFe$_2$O$_4$, causing all organic peaks to disappear. The ZF7 and ZF8 nanofibers display absorption bands at around 530 cm^{-1}, corresponding to the intrinsic stretching vibrations of the metal at the tetrahedral site (Fe↔O), typically observed in the range of 620–500cm^{-1} [22–24]. Specifically, the bands observed at 529 and 530 cm^{-1} for ZF7 and ZF8 are attributed to the Fe↔O stretching vibration of ZnFe$_2$O$_4$. The wave numbers and their corresponding bands are given in **Table 1**.

Table 1 Distinctive IR Absorptions and Corresponding Functional Groups Identified in as-spun and Zinc Ferrite Fibers.

| Sample Code	Wave number (cm^{-1})	Vibration mode	Ref
As-spun fibers	824 1634 1287 3245	Aromatic C–H group of PVP Stretching vibration of C = O of PVP C–N stretching of PVP O-H stretching vibration of PVP	19 18 19 18
ZF7	530	Fe ↔ O stretching vibration	20
ZF8	529	Fe ↔ O stretching vibration	20

The surface morphologies of the as-spun precursor fibers, ZF7 and ZF8 nanofibers, are shown in **Fig. 1(c-e).** The SEM images depict the formation of continuous, bead-free fibers. The average fiber diameter of the as-spun, ZF7, and ZF8 nanofibers are 540, 380, and 347 nm, respectively. The reduction in fiber diameter is attributed to eliminating PVP and removing residual nitrates during the formation of dense crystalline ZnFe$_2$O$_4$ samples.

To confirm dense crystallinity, **Fig. 1(f &g)** presents the TEM images of highly crystalline NF8 nanofibers, showcasing the formation of continuous fibers with an average diameter of 302 nm. In **Fig. 1(h),** the planar distance is measured to be 0.25 nm, corresponding to a spinel ferrite's (311) plane. The SAED pattern typically displays well-defined concentric diffraction rings, indicating the polycrystalline nature of the sample (see **Fig. 1(i)**). The EDAX analysis confirms the purity of the sample. It reveals the presence of Zn (10.19 at. %), Fe (21.83 at. %), and O (67.98 at. %) in ZnFe$_2$O$_4$, consistent with the stoichiometry ratio of Zn: Fe as 1:2. Moreover, the morphology and roughness parameters of ZF8 nanofibers are examined through AFM, as shown in **Fig. 1(j)**. The roughness

parameter is measured to be 20 nm, while the average fiber diameter is 341 nm. These diameter values obtained from AFM closely correspond to the results observed using SEM and TEM. **Fig. 1(k)** presents the M-H curves for ZF7 and ZF8 nanofibers, measured at room temperature under a maximum applied field of 15 kOe. The sharp and narrow hysteresis loops, characterized by minimal coercivity (H_c) and retentivity (M_r), highlight the soft ferromagnetic behavior of the samples. The low-field response is magnified and shown in the inset of Fig. 1(k). Notably, the ZF8 sample demonstrates a peak magnetization of 2.58 emu/g, outperforming ZF7. A comparable report was noted, which indicated a magnetization value of 2.3 emu/g, as reported by Prabhakaran et al.[19].

3.2 Structural analysis and surface morphology of fiber mats

The XRD pattern in **Fig. 2(a)** demonstrates the disappearance of the α-crystalline phase at a 2θ value of 18.6° (110) in PZ15 samples, accompanied by an increase in the intensity of the β-crystalline peak at 2θ value of 20.6°. Additional crystalline peaks observed between 30° to 65° correspond to the crystalline bands of $ZnFe_2O_4$ [25,26].
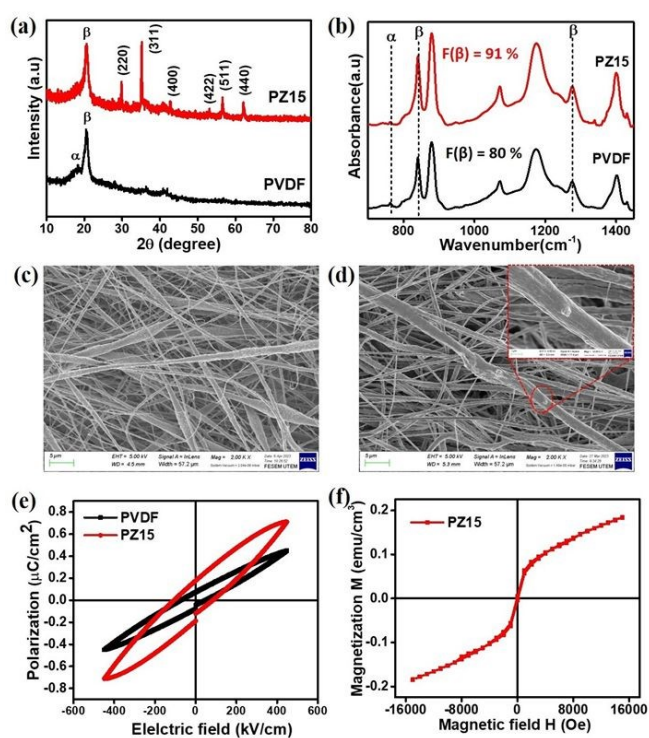
Fig. 2: Structural analysis of PVDF and ZF15 fibers composites. (a) XRD, and (b) FTIR spectra. Surface morphology of (c) PVDF, and (d) ZF15 fibers. (e) P-E loops of PVDF and ZF15 fibers and (f) M-H loop of ZF15 fibers.

In **Fig. 2(b)**, the vibrational bands at 1276 cm^{-1} and 840 cm^{-1} are assigned to the pure β-(TTTT) crystalline phase, while the band at 763 cm^{-1} is assigned to the α-(TGTG) crystalline phase [27]. Notably, the absorbance intensity of the 1276 cm^{-1} and 840 cm^{-1} bands increases in the PZ15 samples compared to neat PVDF, while the intensity of the 763 cm^{-1} band decreases. This suggests a transformation of the α-(TGTG) crystalline phases into the β-(TTTT) phase. The percentage fraction of β-phase was quantitatively determined using the following equation [28]:

$$F_{(\beta)} = \frac{A_{(840)}}{\left(\frac{k_{840}}{k_{763}}\right)A_{(763)} + A_{(840)}} \times 100\% \quad (1)$$

where $A_{(840)}$ and $A_{(763)}$ are the absorbance intensities at 840 cm^{-1} and 763 cm^{-1}, while k_{840} (7.7x10^4 cm^2/mol) and k_{763} (6.1x10^4 cm^2/mol) are their respective adsorption coefficient constants [29]. In Equation 1, the β (840 cm^{-1}) and α (763 cm^{-1}) values correspond to key vibrational modes of PVDF, commonly used to estimate the electroactive β-phase fraction. Other peaks also provide insights into phase composition. The β-phase, responsible for enhanced ferroelectricity, is further confirmed by peaks at 1275 cm^{-1} (C–F stretching) and 510–530 cm^{-1} (skeletal bending), while the α-phase, a non-ferroelectric form, exhibits peaks at 614 cm^{-1} (CH$_2$ twisting), 766 cm^{-1} (CF$_2$ bending), and 976 cm^{-1} (C–C stretching). These peaks help in phase quantification, and their analysis using FTIR and XRD ensures accurate estimation of β-phase content and structural organization in PVDF-based composites[30]. According to Equation 1, the calculated $F_{(\beta)}$ for the PZ15 sample is 91%, compared to 80% for neat PVDF. This enhancement in the electroactive phase is attributed to the effective nucleation process and induced polarization caused by the electrostatic interaction between ZF8 and PVDF. The surface morphology of electrospun nanofibers, shown in **Figs 2(c) & 2(d)**, reveals a uniform, bead-free fiber structure across all samples, irrespective of filler and its composition, indicating the controlled electrospinning conditions followed in this study. The inset in **Fig. 2(d)** further confirms the adherence of ZF8 fibers to the surface of PVDF nanofibrous.

3.3 Ferroelectric and magnetic studies of fibers composites

At room temperature, P-E hysteresis loops were recorded for both neat PVDF film and PZ15 composite fibers, as shown in Fig. 2(e). The neat PVDF film displayed a polarization value of 0.45 μC/cm², while the PZ15 composite demonstrated enhanced ferroelectric behavior, with a maximum polarization of 0.72 μC/cm². The modest increase in polarization values could be influenced by factors such as electrode contact resistance, leakage currents, or incomplete dipole reorientation, which are common in ferroelectric measurements. The electrostatic interactions between the surface charges of $ZnFe_2O_4$ nanofibers and the polar functional groups of PVDF can contribute to this enhancement by facilitating dipole alignment and stabilizing the β-phase [31]. Although techniques like XPS and PFM provide direct confirmation, alternative methods can support this claim. FTIR spectroscopy can reveal an increased β-phase fraction through enhanced absorption at 840 cm^{-1}, while dielectric spectroscopy can indicate improved dipole alignment by analyzing changes in permittivity and loss tangent. XRD can further support phase stabilization by detecting shifts in diffraction peaks associated with β-phase formation. Additionally, P-E hysteresis loop measurements can reveal improved ferroelectric behavior with reduced leakage and enhanced remanent polarization. These complementary characterizations provide scientific evidence supporting the role of electrostatic interactions in the observed polarization enhancement. The incorporation of ZF8 into PVDF promotes the TTTT all-trans planar zigzag conformation, leading to the formation of a ferroelectric/polar orthorhombic structure. This improvement in the ferroelectric loop with ZF8 loading can be attributed to the electrostatic interactions between the surface

charges of $ZnFe_2O_4$ nanofibers and the polar functional groups of PVDF, facilitating the development of the electroactive β-phase [32]. Additionally, the M-H plot of PZ15, shown in **Fig. 2f,** confirmed the presence of magnetic properties in the composite fibers at room temperature. The PZ15 exhibited a soft antiferromagnetic nature, with a maximum magnetization value of 0.19 emu/cm³. These results demonstrate that the PZ15 sample exhibits both ferroelectric and magnetic behaviors at room temperature, indicating its ME nature, which makes it suitable for harvesting mechanical and stray magnetic energies.

3.4. Harvesting Performance of MME Generators

Fig. 3(a) depicts the fabrication of an MME generator constructed using aluminum (Al) as both the top and bottom electrodes, with an ME composite layer (PVDF/ZF8 fibers) serving as the active material. The structure is encapsulated within polyethylene terephthalate (PET) sheets, which can withstand UV rays and have more durability, and designed in a cantilever configuration. One end of the cantilever structure is fixed to a rigid support, while a proof mass is attached to the other, as illustrated in **Fig. 3(b).** The performance of the MME generator was evaluated using a Helmholtz coil, which simulates stray noise magnetic fields akin to those near electrical cables. Optical images of the fabricated MME generator and the flexible ME composite are provided in **Fig. 3(c).** The performance of the MME generator was analyzed over a frequency range of 35 Hz to 70 Hz (**Fig. 3(d)**). By adjusting the proof mass position, the generator was tuned to achieve maximum output at its resonance frequency of 50 Hz (**Fig. 3(e)**).
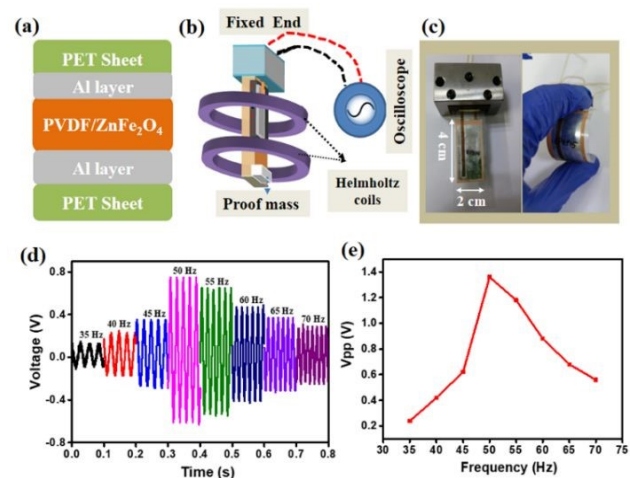
Fig. 3: (a) Fabrication of MME device, (b) Measurement setup, (c) Optical images of MME. (d-e) frequency dependent output voltage and their quantitative plot respectively.

Fig. 4(a) demonstrates the output performance of the MME generator when exposed to a 6 Oe AC magnetic field at 50 Hz. The device based on neat PVDF produced an output voltage of 1.8 V, while the ME composite (PZ15)-based generator delivered a significantly enhanced output voltage of 7.8 V. This performance improvement is attributed to the high β-phase content and the synergistic piezoelectric and ME properties of the composite fibers.

The significant improvement in output voltage (7.8 V compared to the neat PVDF-based generator) can be attributed to several factors. First, the enhanced β-phase formation in the PVDF matrix, facilitated by the incorporation of $ZnFe_2O_4$ nanofibers, leads to improved piezoelectric properties. The β-phase is the electroactive form of PVDF, and its increase directly enhances the material's polarization and energy conversion efficiency, as supported by XRD and FTIR analyses [33]. Additionally, the electrostatic interaction between the $ZnFe_2O_4$ nanofibers and the polar functional groups of PVDF promotes dipole alignment, further improving the overall electroactive response. This alignment is critical for the enhanced piezoelectric and magnetoelectric coupling observed in the composite structure.

The ME voltage coefficient (α_{MME}) was calculated for the MME generators under zero-bias DC magnetic field conditions using the relation [34]:

$$\alpha_{MME} = \frac{V_O}{t * H_{AC}} \qquad (2)$$

where V_0 is the RMS output voltage, t is the thickness of the electrospun composite fibers, and H_{AC} indicates the AC magnetic field. The PZ15-based MME generator achieved an α_{MME} value of 130 V cm⁻¹ Oe⁻¹, approximately four times higher than the neat PVDF-based generator (33 V cm⁻¹ Oe⁻¹).
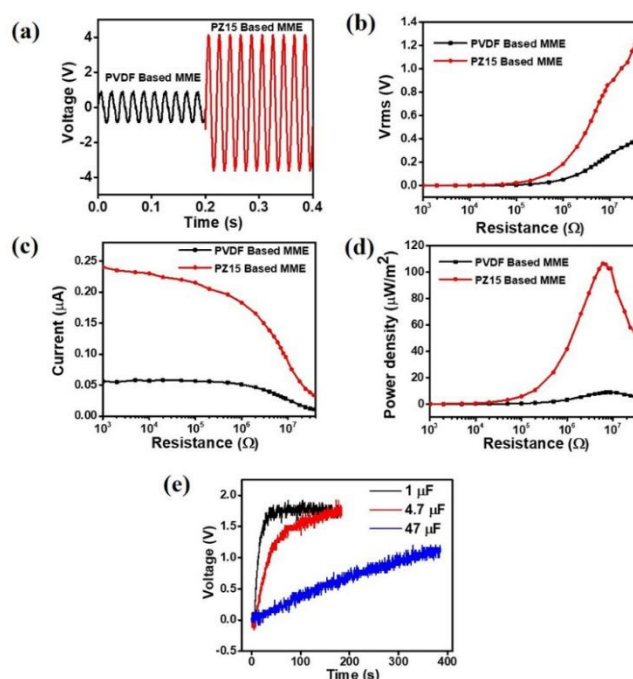
Fig. 4: (a) Output voltage signals generated by the MME generators. (b) V_{rms} and (c) I_{rms} measured across variable load resistances. (d) Power density plot of the MME generators. (e) Capacitor charging curves using the electrical energy generated by the PZ15-based MME generator.

The AC output voltage signals were converted to DC signals using a full-bridge rectifier circuit. RMS voltage and current measurements under varying external load conditions (10 kΩ to 36 MΩ) are

presented in **Fig. 4(b) - 4(d).** The recorded RMS voltage values were 0.39 V for the PVDF-based generator and 1.2 V for the PZ15-based generator. Correspondingly, the power density outputs at an optimal load resistance of ~6 MΩ were calculated to be 9 μW/m² for the PVDF-based generator and 106 μW/m² for the PZ15-based generator (**Fig. 4(d)**). The energy harnessed by the PZ15-based MME generator is stored in capacitors with capacitances of 1 μF, 4.7 μF, and 47 μF, as shown in **Fig. 4(e)**. After charging for 100 s, 160 s, and 330 s, the capacitors reached stable voltage levels of 1.78 V, 1.72 V, and 1.1 V, respectively. These results highlight the effective energy storage capability of the designed PZ15-based MME generator.

To evaluate the effectiveness of the device as a magnetic sensor, we tested the performance of the PZ15-based MME generator under various magnetic field conditions. The real-time magnetic sensitivity of the device is characterized by measuring its output voltage in response to incident magnetic fields ranging from 200 μT to 50 μT. The device demonstrated stable output voltage performance down to an AC magnetic field of 50 μT, as shown in **Fig. 5(a). Fig. 5(b)** depicts the corresponding peak-to-peak output voltage, revealing a linear relationship between the magnetic field strength and the output voltage, which is a desirable characteristic for magnetic sensors[35]. Additionally, we evaluated the real-time energy harvesting capability of the PZ15-based MME generator by detecting small magnetic noise fields emitted by household appliances' power cables (see **Fig. 5(c)**). The device was placed near the power cords of a hairdryer, electric heater, and microwave oven, generating output voltages of 2.6 V, 3 V, and 4.1 V, respectively, as illustrated in **Fig. 5(d).** Based on the magnetic sensing data, the field strengths near the cables were estimated to be approximately 3.4 Oe, 4.0 Oe, and 5.5 Oe, respectively.
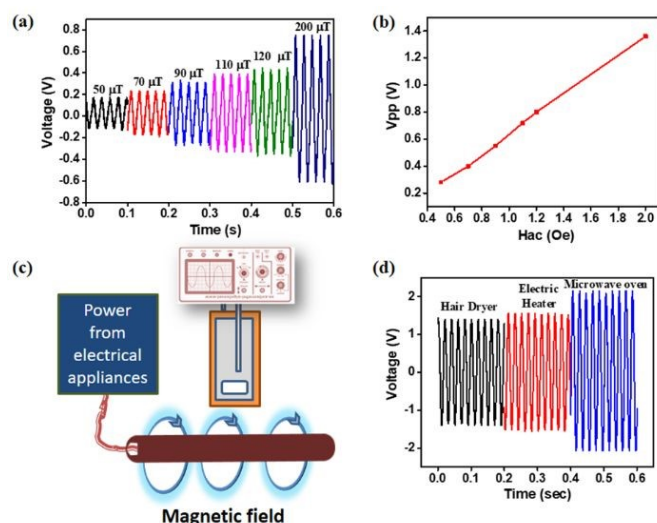

Fig. 5: (a-b) output voltage derived at different magnetic field and their quantitative plot respectively, (c-d) demonstration of MME energy harvesting, and it's output voltage.

We have developed a multi-mode energy harvesting system that utilizes electromagnetic hybridization. This is achieved by positioning a solenoid coil near the permanent magnets at the end of the MME

setup, as depicted in **Fig. 6(a)**. The movement between the magnet and the coil at the end of the cantilever causes changes in magnetic flux due to the vibrations of the MME device. According to Faraday's law of electromagnetic induction, the generated electromotive force (emf) can be expressed as $\varepsilon = - (d\varphi/dt)$, where φ is the magnetic flux that is perpendicular to the coil, and t represents time [36,37]. The induced emf in a closed loop corresponds to the rate of change of magnetic flux through that loop over time. As illustrated in **Fig. 6(b),** the open-circuit voltage output measured from the electromagnetic components of the multi-mode device gradually increases with the intensity of the magnetic field generated by the AC Helmholtz coils, reaching a maximum of 2.94 V at a magnetic field strength of 6 Oe.

This increase in voltage output occurs because a higher rate of change in magnetic flux results in a greater induced emf in the coil. In addition, a coin-dropping experiment is conducted to evaluate the piezoelectric output of the device. **Fig. 6 (c)** presents the schematic of the piezoelectric sensor (PZ15 fibers composite) subjected to coins with various weights dropped from a height of 15 cm. The corresponding output voltage signals are shown in **Fig. 6 (d).** The results indicate that the voltage output exhibits a linear response as the load is varied from 3.5 g to 18.5 g, with a maximum output voltage of 2.6 V observed at an 18.5 g load. This linearity highlights the effectiveness of the device as a stress sensor.
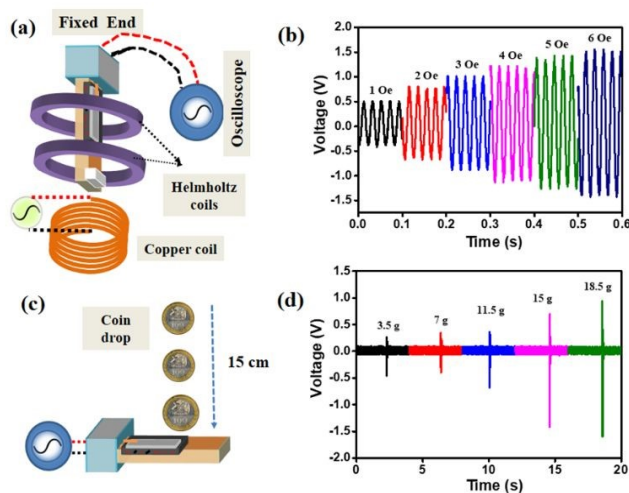
Fig. 6: Multimode energy harvesting: (a) schematic structure, (b) output voltage from electromagnetic energy harvesting, (c) coin drop experiment, and (d) corresponding output voltage signals.

Conclusions

In this study, we successfully developed hybrid multi-mode energy generators using PVDF/ZnFe$_2$O$_4$ ME composite fibers. These fibers were fabricated using the electrospinning technique, yielding uniform, bead-free structures as confirmed by FE-SEM analysis. Integrating high-aspect-ratio ZnFe$_2$O$_4$ fillers into the PVDF matrix promoted the formation of the ferroelectric β-phase through electrostatic interactions, as validated by XRD and FTIR analyses. The composite fibers exhibited multiferroic properties, demonstrated by P-E hysteresis loop and M-H hysteresis loop measurements. The

MME generators constructed with these composites achieved output voltages of 1.8 V for the PVDF-based generator and 7.8 V for the PZ15-based generator. Additionally, a voltage of 2.94 V is generated using the electromagnetic hybridization process in the MMME generator. Furthermore, the devices demonstrated energy storage capabilities, successfully charging capacitors with capacitances of 1 µF, 4.7 µF, and 47 µF. This PZ15-based generator showcased effective power generation through reliable energy harvesting from various household electrical appliances and enabled magnetic field sensing across a range from 200 µT down to 50 µT. Our findings highlight the versatility of the developed device, which combines electromagnetic and piezoelectric mechanisms for enhanced functionality. The developed PZ15-based multi-mode energy generator shows significant potential for powering self-sustained devices in applications such as smart electronics, wearable technology, and environmental monitoring. This research paves the way for innovative advancements in multi-mode energy harvesting solutions.

Author contributions

Durga Prasad Pabba: Writing – original draft, Methodology, Software, Nayak Ram: Data curation, Writing – review & editing, J. Kaarthik: Writing – review & editing, Vijayabhaskara Rao Bhaviripudi: Writing – review & editing, Sandeep Kumar Yadav: Writing – review & editing, M. Satthiyaraju: Writing – review & editing, R.V. Mangalaraja: Writing – review & editing, Radhamanohar Aepuru: Writing – review & editing, Validation, Funding acquisition, Annapureddy Venkateswarlu: Conceptualization, Methodology, Funding acquisition, Validation, Writing – review & editing.

Conflicts of interest

There are no conflicts to declare.

Data availability

Data will be available based on the request.

Acknowledgments

Notes and references

1   S. Lee, C. M. Baek, G. H. Kim, S. Pattipaka, H. Song, J. Jang, G.-T. Hwang and J. Ryu, *Advanced Science*, **n/a**, 2405526.

2   Y. Yu, Z. Cheng, J. Chang, Z. Mai, B. Wang, R. Zhu, M. Sun, S. Dong and P. Ci, *Advanced Energy Materials*, **n/a**, 2402487.

3   Z. Yu, J. Yang, L. Xu, J. Chang, Z. Li, X. Yuan and S. Dong, *Energy Environ. Sci.*, DOI:10.1039/D3EE03634K.

4   D. Choi, Y. Lee, Z.-H. Lin, S. Cho, M. Kim, C. K. Ao, S. Soh, C. Sohn, C. K. Jeong, J. Lee, M. Lee, S. Lee, J. Ryu, P. Parashar, Y. Cho, C. Ahn, I.-D. Kim, F. Jiang, P. S. Lee, G. Khandelwal, S.-J. Kim, H. S. Kim, H.-C. Song, M. Kim, J. Nah, W. Kim, H. G. Menge, Y. T. Park, W. Xu, J. Hao, H. Park, J.-H. Lee, D.-M. Lee, S.-W. Kim, J. Y. Park, H. Zhang, Y. Zi, R. Guo, J. Cheng, Z. Yang, Y. Xie, S. Lee, J. Chung, I.-K. Oh, J.-S. Kim, T. Cheng, Q. Gao, G. Cheng, G. Gu, M. Shim, J. Jung, C. Yun, C. Zhang, G. Liu, Y. Chen, S. Kim, X. Chen, J. Hu, X. Pu, Z. H. Guo, X. Wang, J. Chen, X. Xiao, X. Xie, M. Jarin, H. Zhang, Y.-C. Lai, T. He, H. Kim, I. Park, J. Ahn, N. D. Huynh, Y. Yang, Z. L. Wang, J. M. Baik and D. Choi, *ACS Nano*, 2023, **17**, 11087–11219.

5   V. Annapureddy, H. Palneedi, G.-T. Hwang, M. Peddigari, D.-Y. Jeong, W.-H. Yoon, K.-H. Kim and J. Ryu, *Sustainable Energy Fuels*, 2017, **1**, 2039–2052.

6   V. Annapureddy, S.-M. Na, G.-T. Hwang, M. G. Kang, R. Sriramdas, H. Palneedi, W.-H. Yoon, B.-D. Hahn, J.-W. Kim, C.-W. Ahn, D.-S. Park, J.-J. Choi, D.-Y. Jeong, A. B. Flatau, M. Peddigari, S. Priya, K.-H. Kim and J. Ryu, *Energy Environ. Sci.*, 2018, **11**, 818–829.

7   J. Ryu, J.-E. Kang, Y. Zhou, S.-Y. Choi, W.-H. Yoon, D.-S. Park, J.-J. Choi, B.-D. Hahn, C.-W. Ahn, J.-W. Kim, Y.-D. Kim, S. Priya, S. Y. Lee, S. Jeong and D.-Y. Jeong, *Energy Environ. Sci.*, 2015, **8**, 2402–2408.

8   M. S. Kwak, M. Peddigari, H. Y. Lee, Y. Min, K.-I. Park, J.-H. Kim, W.-H. Yoon, J. Ryu, S. N. Yi, J. Jang and G.-T. Hwang, *Advanced Functional Materials*, 2022, **32**, 2112028.

9   D. P. Pabba, N. Ram, J. Kaarthik, V. R. Bhaviripudi, S. K. Yadav, A. Soosairaj, N. K. Pabba, V. Annapureddy, A. Thirumurugan, H. S. Panda and R. Aepuru, *Ceramics International*, DOI:10.1016/j.ceramint.2024.06.115.

10 N. Ram, J. Kaarthik, S. Singh, H. Palneedi, P. D. Prasad and A. Venkateswarlu, *Ceramics International*, 2024, **50**, 17465–17474.

11 N. Ram, D. P. Pabba, J. Kaarthik, G. Hwang, K. Vaduganathan and A. Venkateswarlu, *Advanced Sustainable Systems*, 2024, 2400548.

12 S. Bera, S. Ojha, P. Maity, N. L. Sengupta and B. B. Khatua, *Journal of Alloys and Compounds*, 2024, **1005**, 176038.

13 D. P. Pabba, B. V. B. Rao, A. Thiam, A. Thirumurugan, V. Meruane, R. Aepuru and H. J, *Ceramics International*, 2024, **50**, 4178–4189.

14 S. Ponnan, C. L. C S, M. S. Reza, S. Moozhiyil Purushothaman, M. Fernandes-tronco, M. Poncot, H. Kim, S. Thomas, I. Royaud, D. Rouxel and N. Kalarikkal, *ACS Appl. Electron. Mater.*, 2024, **6**, 4963–4976.

15 J. Kaarthik, N. Ram, R. Aepuru, S. G. Reddy, D. P. Pabba and A. Venkateswarlu, *Sustainable Energy Fuels*, 2024, **8**, 2583–2592.

16 L. Ruan, X. Yao, Y. Chang, L. Zhou, G. Qin and X. Zhang, *Polymers*, 2018, **10**, 228.

17 J. Wang, G. Yang, L. Wang and W. Yan, *Electrochimica Acta*, 2016, **222**, 1176–1185.

18 M. Arias, V. M. Pantojas, O. Perales and W. Otaño, *Journal of Magnetism and Magnetic Materials*, 2011, **323**, 2109–2114.

19 T. Prabhakaran and J. Hemalatha, *sci adv mater*, 2014, **6**, 1313–1321.

20 V. C. Agulto, M. J. F. Empizo, K. Kawano, Y. Minami, K. Yamanoi, N. Sarukura, A. C. C. Yago and R. V. Sarmago, *Optical Materials*, 2018, **76**, 317–322.

21 K. M. Koczkur, S. Mourdikoudis, L. Polavarapu and S. E. Skrabalak, *Dalton Trans.*, 2015, **44**, 17883–17905.

RSC Applied Polymers Accepted Manuscript

22 M. V. Limaye, S. B. Singh, R. Das, P. Poddar, M. K. Abyaneh and S. K. Kulkarni, *Journal of Magnetism and Magnetic Materials*, 2017, **441**, 683–690.

23 M. Vadivel, R. Ramesh Babu, K. Sethuraman, K. Ramamurthi and M. Arivanandhan, *Journal of Magnetism and Magnetic Materials*, 2014, **362**, 122–129.

24 P. Durga Prasad and J. Hemalatha, *Physica B: Condensed Matter*, 2019, **573**, 1–6.

25 L. Li, M. Zhang, M. Rong and W. Ruan, *RSC Adv.*, 2013, **4**, 3938–3943.

26 Farhan, S. Ahmad, H. Ullah, Z. U. Rehman, M. Nawaz, I. Uddin, A. Parkash, H. R. Alamri, N. S. Alsaiari and M. S. Javed, *Nanomaterials*, 2022, **12**, 2796.

27 J. Zhu, C. Chen and R. Zhang, *Applied Surface Science Advances*, 2021, **5**, 100115.

28 S. Ponnan, T. W. Schmidt, T. Li, H. B. Gunasekaran, X. Ke, Y. Huang, S. Mubarak, A. Anand Prabu, Z. Weng and L. Wu, *ACS Appl. Polym. Mater.*, 2021, **3**, 4879–4888.

29 M. T. Rahman, S. S. Rana, M. A. Zahed, S. Lee, E.-S. Yoon and J. Y. Park, *Nano Energy*, 2022, **94**, 106921.

30 C. Bahloul, S. Ez-Zahraoui, A. Eddiai, O. Cherkaoui, M. Mazraoui, F.-Z. Semlali and M. El Achaby, *RSC Adv.*, 2024, **14**, 38872–38887.

31 H. Parangusan, K. Karuppasamy and J. Bhadra, *Journal of Alloys and Compounds*, 2024, **989**, 174254.

32 A. Bhiogade, K. Nagamalleswari, P. Mandal and V. K. M. Ramakrishnan, *J Mater Sci*, 2023, **58**, 17805–17815.

33 M. M. Hussein, S. A. Saafan, H. F. Abosheiasha, D. Zhou, D. I. Tishkevich, N. V. Abmiotka, E. L. Trukhanova, A. V. Trukhanov, S. V. Trukhanov, M. K. Hossain and M. A. Darwish, *Materials Chemistry and Physics*, 2024, **317**, 129041.

34 S. H. Park, A. Kumar, J. Kaarthik, V. Annapureddy and J. Ryu, *Electronic Materials Letters*, 2020, **16**, 369–375.

35 V. Annapureddy, H. Palneedi, W.-H. Yoon, D.-S. Park, J.-J. Choi, B.-D. Hahn, C.-W. Ahn, J.-W. Kim, D.-Y. Jeong and J. Ryu, *Sensors and Actuators A: Physical*, 2017, **260**, 206–211.

36 P. Neamatollahi, S. Abrishami, M. Naghibzadeh, M. H. Yaghmaee Moghaddam and O. Younis, *IEEE Trans. Ind. Inf.*, 2018, **14**, 1876–1886.

37 M. Cheng, J. Wu, X. Liang, R. Mao, H. Huang, D. Ju, Z. Hu, J. Guo and M. Liu, *Sensors and Actuators A: Physical*, 2023, **352**, 114194.

Data Availability Statement

The data will be available on request.